THE JOURNAL OF PHYSICAL CHEMISTRY C

ARTICLE

pubs.acs.org/JPCC

Investigations of Formation of Molecular Sieve SAPO-34

Lu Zhang,[†] Jennifer Bates,[†] Donghan Chen,[†] Heng-Yong Nie,[‡] and Yining Huang*[,†]

[†]Department of Chemistry, and [‡]Surface Science Western, The University of Western Ontario, London, Ontario N6A 5B7, Canada

Supporting Information

ABSTRACT: Crystallization of a catalytically important molecular sieve SAPO-34 was examined under dry gel conversion conditions including steam-assisted conversion (SAC) and vapor-phase transport (VPT). The progressive changes in the structure of solid gel phases were monitored by powder XRD, SEM, and several solid-state NMR techniques involving ^{31}P, ^{27}Al, ^{29}Si, and ^{13}C. The results suggest that the formation pathways under VPT and SAC appear to be similar: SAPO-34 crystallizes from a semicrystalline precursor with a layered structure held mainly by weak nonbonding interactions. AFM data indicate that the crystal growth mechanism is "birth and spread" and that the fast nucleation on the (001) crystal face likely results from simultaneous transformation of many small domains of precursor to SAPO-34 via cooperative bond breaking and reforming. ^{29}Si NMR results suggest that Si incorporation occurs slowly via amorphous aluminosilicate species. These findings provide new physical insights into the formation of SAPO-34.

INTRODUCTION

Zeolites have been extensively used in industry as ion-exchangers, sorbents, and, in particular, catalysts. Another important type of microporous materials is aluminophosphate ($AlPO_4$)-based molecular sieves.[1] Unlike zeolites whose frameworks are negatively charged, $AlPO_4$-based molecular sieves have neutral frameworks and therefore cannot be directly used as acidic catalysts. However, introducing Si into the $AlPO_4$ frameworks yields negatively charged frameworks. Therefore, the resulting silicoaluminophosphates (SAPOs) can be used as catalysts for several reactions catalyzed by acids.

Among SAPO-based catalysts, SAPO-34 is of particular importance. It has CHA topology (Scheme 1).[2] The framework contains chabazite (CHA) cages, which can be accessed via an eight-membered ring (8R) window with a pore diameter of ~0.38 nm. SAPO-34 has shown potentials for several applications including gas separation and water adsorption.[3,4] Perhaps, the most important use of this material is to catalyze the methanol-to-light olefin reactions.[5−10] SAPO-34-based catalysts have been used commercially to convert methanol to ethylene and propylene. The catalytic performance is determined by the Si content and distribution within the framework, and these factors are often influenced by the synthetic conditions and the structure-directing agent (SDA) used. The formation of SAPO-34 under hydrothermal synthesis (HTS) conditions has been studied with various SDAs.[11−19] Since the early work by Liu and co-workers,[15,18] diethylamine (DEA) has increasingly become a choice of SDA due to its ability of producing SAPO-34 with high thermal stability, high Si content, and high crystallinity as well as its relatively low cost. Despite that the crystallization of SAPO-34 with DEA as SDA has been examined, its formation on a molecular level is still not completely understood.

One of the alternative methods for SAPO synthesis is dry gel conversion (DGC).[20−30] This method involves treating predried gel powder at elevated temperatures and autogenous pressures to form crystalline molecular sieves. The DGC synthesis can be carried out in two ways: (i) steam-assisted conversion (SAC) where the initial dry gel containing SDA is separated from a small amount of water in an autoclave and (ii) vapor-phase transport (VPT), which is similar to SAC except that a small amount of SDA solution/liquid is put at the bottom of an autoclave (Scheme 2). The differences and similarities in crystallization under DGC and HTS conditions have been discussed by several authors.[31,32] The predried gel powder usually contains 20−40% water by weight. The water occluded inside the "dry" gel and the water initially placed at the bottom of an autoclave have been found to play a critical role in crystallization.[31,32] It is recognized that the mechanisms underlying the crystallization under the DGC and HTS conditions may be fundamentally similar. The lack of apparent liquid phase, however, does limit mass transport and therefore may result in lower crystal growth rates. Consequently, the intermediates may be obtained under the favorable circumstances.

In the present work, SAPO-34 crystallization under both SAC and VPT conditions has been investigated by using diethylamine as a SDA. Attention was also placed in Si incorporation. Evolution of long-range ordering in the dry gel was followed by powder X-ray diffraction (PXRD); the changes in gel morphology were monitored by scanning electron microscopy (SEM); the development of short-range ordering of framework elements was probed by ^{31}P, ^{27}Al, and ^{29}Si magic-angle spinning (MAS)

Received: September 5, 2011
Revised: October 10, 2011
Published: October 12, 2011

Scheme 1. Framework of SAPO-34

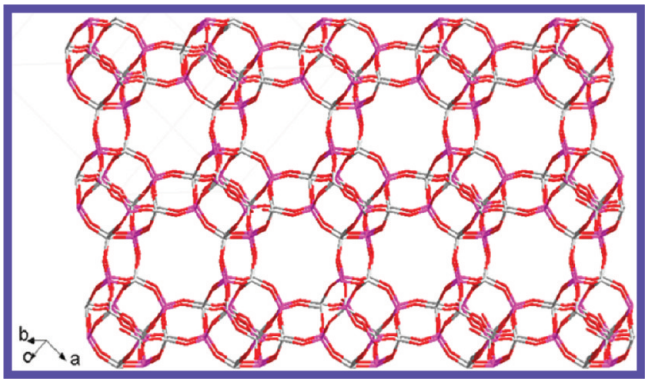

Scheme 2. Diagram of the Reaction Vessel Used for the DGC Method

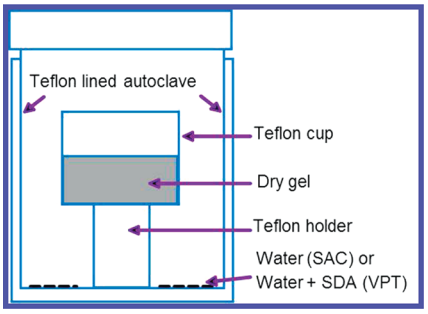

NMR; and the behavior of SDA was examined by ^{13}C NMR. Different Al species in the gel were differentiated by ^{27}Al triple quantum MAS (3QMAS) NMR. The P−O−Al connectivity was established by $^{31}P\{^{27}Al\}$ and $^{27}Al\{^{31}P\}$ rotational-echo double-resonance (REDOR) experiments. Si incorporation was investigated by $^{1}H \rightarrow {}^{29}Si$ cross-polarization (CP) NMR. Further, the nucleation and growth were examined by atomic force microscopy (AFM). From the data obtained from these techniques, some new insights into the SAPO-34 formation process were obtained.

EXPERIMENTAL SECTION

Sample Preparation. The reagents used were pseudoboehmite (Catapal-B, Vista, ca. 65% Al_2O_3), H_3PO_4 (EM Science, 85%), diethylamine (Alfa Aesar), colloidal silica (Ludox LS-30, Aldrich), and the remainder was distilled water. The initial dry gel compositions (Al_2O_3:P_2O_5:SiO_2:DEA:H_2O) for SAC and VPT were 1.0:0.8:0.4:2.0:50 and 1.0:0.8:0.4:0:50, respectively. A typical procedure[22] for the preparation of SAC dry gel is the following: 15.7 g of Catapal B was mixed with 76.1 g of distilled water, and the mixture was stirred at room temperature for 10 min followed by adding 18.4 g of H_3PO_4 slowly with continuous stirring. The solution containing 8 g of colloidal silica and 14.6 g of DEA, which was also stirred for 10 min at room temperature, was then added to the above mixture under vigorous stirring for homogeneity. The final mixture was stirred for 1 h and then dried at 353 K with constant stirring to allow evaporation of water until white solids formed. The solid sample was then ground into a fine powder and sealed in glass vials. A series of intermediates were synthesized by placing 1.0 g of the initial SAC dry gel powder into small Teflon cups. Each cup was placed in a 23 mL Teflon-lined autoclave with 0.4 g of distilled water at the bottom and heated in an oven at 473 K for different times. The reactions were quenched in cold water. For comparison, each solid sample was divided into two parts. One part was dried in air, and the other part was first washed with distilled water in a beaker and then dried in the same beaker in air without isolation from the liquid phase. This ensured that solid particles were not washed away. All dried samples were kept in sealed vials for further analysis. For the VPT method, the initial dry gel was prepared similarly to SAC method, but without DEA. Instead, 1.2 g of 25% aqueous DEA solution was placed at the bottom of each autoclave.

Characterization. PXRD patterns were recorded on a Rigaku diffractometer using Co Kα radiation (λ = 1.7902 Å). Morphological investigations and energy dispersive X-ray (EDX) analyses were performed on a LEO 1540XB field emission scanning electron microscope.

All of the NMR experiments were carried out on a Varian/Chemagnetics Infinityplus 400 WB spectrometer equipped with three rf channels operating at the field strength of 9.4 T. The Larmor frequencies of ^{1}H, ^{13}C, ^{31}P, ^{27}Al, and ^{29}Si were 399.5, 100.4, 161.7, 104.1, and 79.4 MHz, respectively. The chemical shifts of ^{13}C, ^{31}P, ^{27}Al, and ^{29}Si were referenced to adamantane, $NH_4H_2PO_4$, 1 M $Al(NO_3)_3$, and tetrakis(trimethylsilyl)-silane (TTMSS). Depending on the requirements of individual experiment, three MAS probes were used (a Varian/Chemagnetics 7.5 mm, a 4.0 mm H/X/Y triple-tuned T3 MAS, and a 5.0 mm H/F/X/Y triple-tuned MAS probe). The ^{13}C CP MAS spectra were recorded by using the 5.0 mm probe with the Hartmann−Hahn conditions set on adamantane, and the ^{1}H 90° pulse length was 4 μs. A contact time of 2 ms was used, and the pulse delay was 9 s. The proton-decoupling field was about 60 kHz. For ^{31}P MAS experiments, a 45° pulse was typically used, and the recycle delay was 60 s. The ^{27}Al spectra were acquired using a 30° pulse with a pulse delay of 1 s. For the ^{29}Si MAS experiments, a 45° pulse was used with a pulse delay of 60 s. For ^{29}Si CP MAS experiments, the ^{1}H 90° pulse length was 5 μs, and the Hartmann−Hahn condition was determined on TTMSS. $^{31}P\{^{27}Al\}$ and $^{27}Al\{^{31}P\}$ REDOR experiments were performed with the 5.0 mm probe with a spinning speed of 8 kHz using the standard REDOR pulse sequence.[33] The details for REDOR experiments were described in a previous work.[34] ^{27}Al 3QMAS experiments were performed using the 4.0 mm probe, and the spinning rate was 10 kHz. The spectra were obtained by utilization of a three-pulse z-filter sequence.[35] The rf strengths of the first two hard pulses and third soft pulse were optimized individually, and the optimized pulse lengths were 5.7, 2.0, and 15.0 μs for the three consecutive pulses.

AFM used in a surface structure study is a Park Systems XE-100. A cantilever with nominal spring constant of 40 N/m, resonant frequency of 300 kHz, and tip radius of 10 nm (NSC15, Mikro Masch) was operated under the dynamic force mode. In this mode, the cantilever is vibrated at around the resonant frequency, and its amplitude reduces when the tip is in proximity with the sample surface caused by the tip−sample interaction. Reduced amplitude is set as the feedback parameter (set point) so that the AFM system scans the surface contour of the sample with minimized error signals (the difference between the set point and the amplitude measured) by adjusting the distance

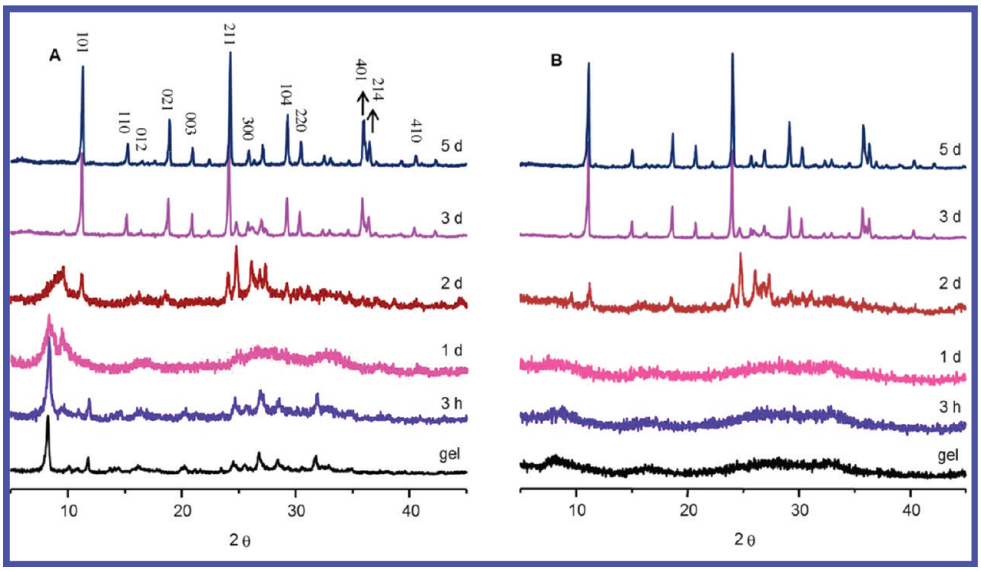

Figure 1. Powder XRD patterns of (A) unwashed and (B) washed SAC dry gel samples.

between the tip and the sample surface. Mapping of this distance constructs topographic image for the surface morphology. Mapping the error signal results in an image removing the height contribution and stressing only the shape of surface features. When the height range is large, surface features with small height differences are obscured. In this case, it is advantageous to use the error signal image to show the shapes of surface features, while using the topographic image to estimate the height distribution. The scan rate for obtaining images in an area of $45 \times 45\ \mu m^2$ is 0.5 Hz and for images in an area of $10 \times 10\ \mu m^2$ is 1 Hz. The experiment was conducted in air with a relative humidity of ~40%.

RESULTS AND DISCUSSION

Formation of SAPO-34 under SAC Conditions. Powder X-ray diffraction was used to monitor the evolution of long-range ordering in SAC gel, and the selected patterns are shown in Figure 1A. The pattern of the unwashed initial SAC dry gel has sharp reflections with a very strong low angle peak, which means that the major component of the initial dry gel is a layered material with long-range ordering. Upon heating, the peaks due to the layered phase gradually become weaker and broader. It appears that the crystalline layered phase became a semicrystalline material. Heating the dry gel for 2 days resulted in the emergence of several sharp peaks whose positions correspond to (101), (211), and (300) reflections of SAPO-34. However, the pattern also contains the peaks due to $AlPO_4$-11, implying that $AlPO_4$-11 is likely a competing phase. Seeing $AlPO_4$-11 is not surprising because DEA is known to template $AlPO_4$-11.[36] Further heating the gel leads to continuing increase in the intensity of the peaks due to SAPO-34 and disappearing of the reflections belonging to $AlPO_4$-11. The pattern of the 5-day sample only contains the peaks solely due to trigonal SAPO-34, and no peak from $AlPO_4$-11 is seen in the pattern.

Previous work[37−40] has shown that the structure of the intermediates formed during the crystallization of SAPO- and AlPO-based molecular sieves under DGC conditions is held by weak, noncovalent bonding interactions. To investigate the nature of the bonding in the SAC gel samples, we washed the intermediates with water. Upon washing, all of the reflections due to the layered phases and the broad reflections due to the semicrystalline layered phase disappeared in the corresponding XRD patterns (Figure 1B). Only broad amorphous halos remained in the washed samples heated for less than 2 days. These findings suggest that the structure of the crystalline and semicrystalline layered phases is also held by the weak hydrogen bonding and/or van der Waals forces.

Several representative samples were chosen for SEM analysis to examine the morphological evolution of SAC gel samples as a function of crystallization time (Figure 2). The image of the initial SAC dry gel exhibits layered morphology. Disordered aggregates were observed after 1 day of heating. The image of 2 d sample shows the formation of SAPO-34 crystals resulting from the transformation of the semicrystalline phase (see Figure 2C). The highly crystalline SAPO-34 product is formed after 5 days. The trend agrees with the XRD result very well.

To characterize the local environments of P and Al atoms in the intermediate phases, ^{31}P and ^{27}Al solid-state MAS NMR spectra were obtained. Figure 3A shows the ^{31}P spectra of unwashed SAC gel samples. The ^{31}P spectrum of the initial dry gel has three sharp peaks at −18.9, −20, and −22.6 ppm, indicating that the crystalline layered phase has, at least, three different P sites. There are also several broader and weaker peaks between 0 and 10 ppm, and they are likely due to a small amount of amorphous material. Upon heating, the three crystallographically nonequivalent peaks gradually become a single peak at around −20 ppm due to the transformation to the semicrystalline intermediate. This peak is broader than those of initial gel, but still relatively narrow, implying that the semicrystalline phase still maintains the ordered local environment around P despite losing long-range ordering. The chemical shift indicates that the P in the layered phase is not fully condensed.[41−43] After 2 days of the SAC treatment, a new peak starts emerging at around −30 ppm, indicating the formation of fully condensed P with $P(OAl)_4$ environment. The spectrum of the final product (5 d sample) only has a single peak at −29.8 ppm, which is consistent with that

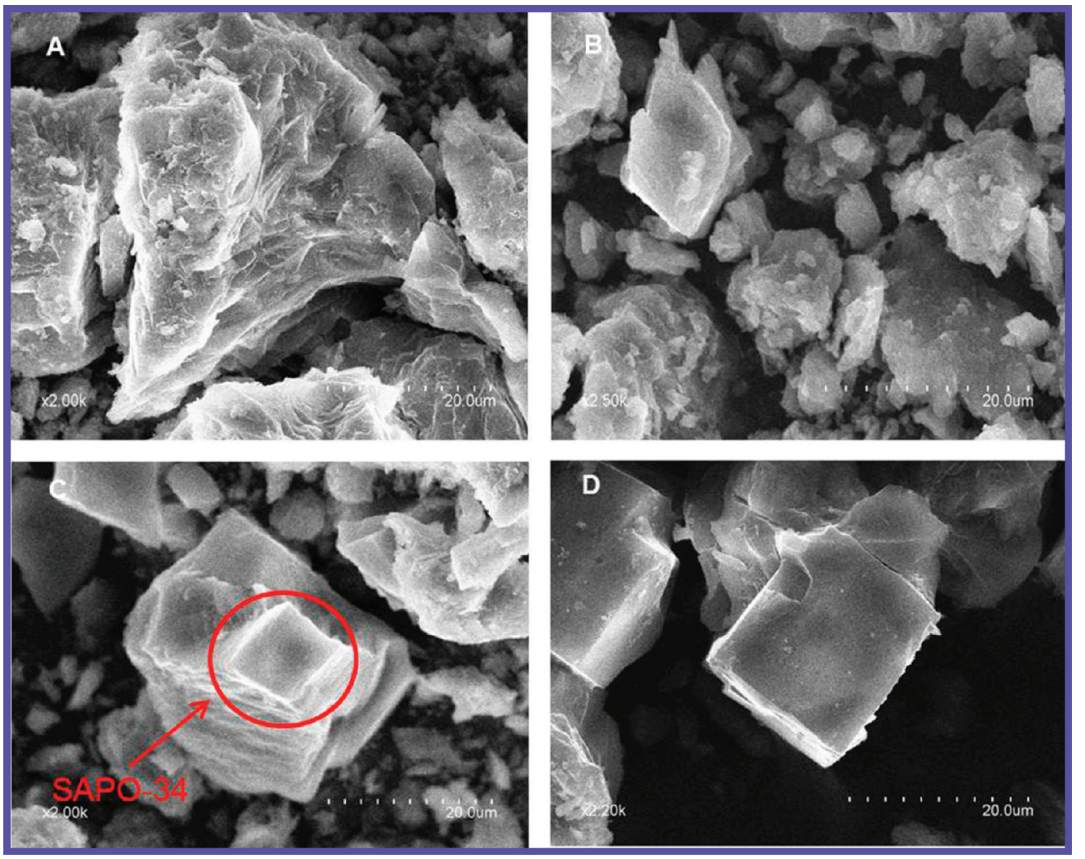

Figure 2. SEM images of unwashed (A) initial dry gel, (B) 1 d, (C) 2 d, and (D) 5 d SAC gel samples.

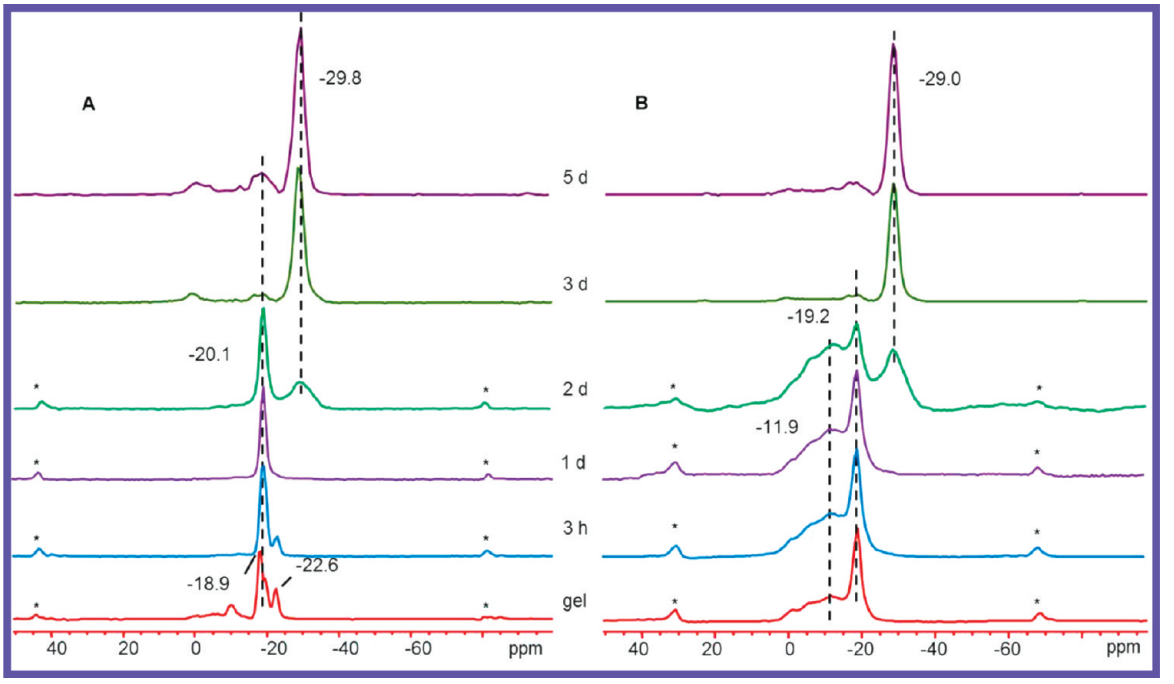

Figure 3. ^{31}P MAS spectra of (A) unwashed and (B) washed SAC dry gel samples. Asterisks indicate spinning sidebands.

trigonal SAPO-34 only has a single T (tetrahedral) site. There are two very weak and broad peaks in the spectrum, suggesting the existence of a small amount of amorphous impurity.

Although we believe that the initial dry gel is AlPO in nature, the possibility that it might be a layered diethylammonium phosphate cannot be ruled out without additional experiment.

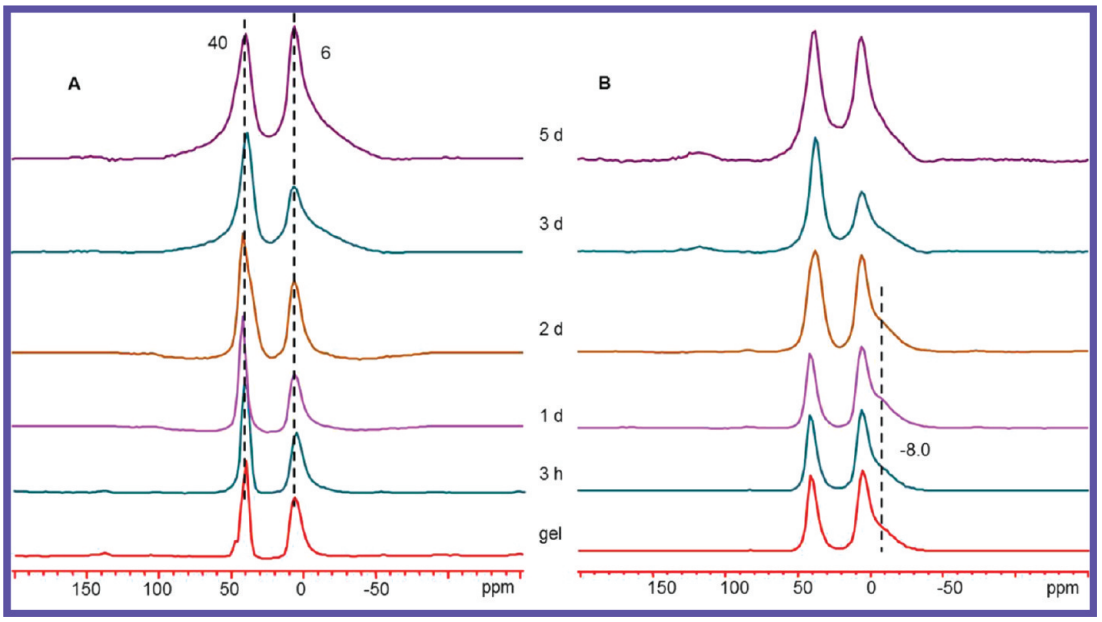

Figure 4. ^{27}Al MAS spectra of (A) unwashed and (B) washed SAC dry gel samples.

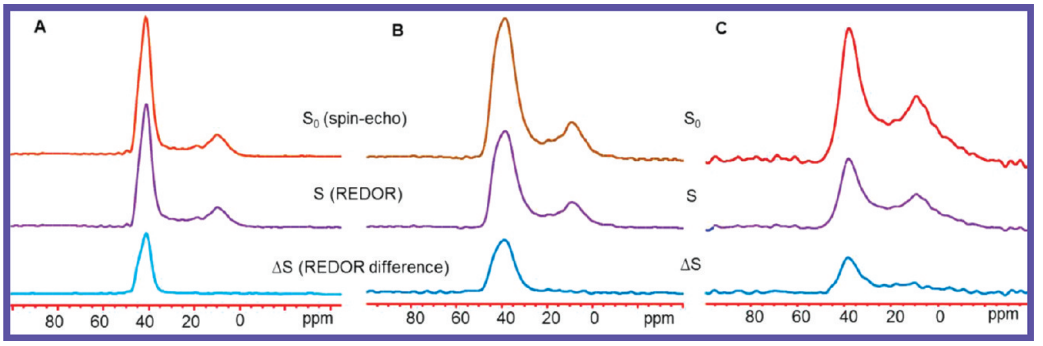

Figure 5. ^{27}Al $\{^{31}P\}$ REDOR spectra of the 3 h (A), 2 d (B), and 5 d (C) samples with a dephasing time of 1.25 ms.

To clarify this situation, we carried out $^{31}P\{^{27}Al\}$ REDOR experiments on 3 h sample, which has a PXRD pattern identical to that of the initial gel. REDOR is a technique designed to detect weak heteronuclear dipolar interaction involving two unlike spins. In the present case, we use $^{31}P\{^{27}Al\}$ REDOR to detect P−O−Al connectivity because only the P dipolar coupled to Al will be seen in the $^{31}P\{^{27}Al\}$ REDOR difference spectrum. Figure S1 show that the P peaks between −19 and −23 ppm appear in the REDOR difference spectra (ΔS), unambiguously confirming that the layered phase is an AlPO material and not an amine phosphate.

The ^{27}Al MAS spectrum of the initial dry gel shows two strong peaks at 40 and 6 ppm (Figure 4A). The 40 ppm peak indicates the existence of tetrahedral Al in the layered phase. The 6 ppm peak is likely due to either unreacted aluminum oxide or 5-coordinated Al with $Al(OP)_4(OH_2)$ environment in AlPO species.[13] The spectra did not change significantly with increasing heating time except that the peaks gradually become broader. The spectrum of the 5 d sample (the final product) is consistent with those reported in the literature.[2] To identify the nature of the 6 ppm peak, we also carried out $^{27}Al\{^{31}P\}$ REDOR experiments on selected samples heated for 3 h, 2 d, and 5 d (Figure 5). For all the samples, the REDOR difference spectra (ΔS in Figure 5) clearly show only the tetrahedral Al peak. The peak at 6 ppm seen in the MAS spectra did not appear in the REDOR difference spectra. These results clearly indicate that this peak is due to unreacted alumina with no P atom in the second coordination sphere. The ^{27}Al 3QMAS spectrum of SAPO-34 (5 d sample) is illustrated in Figure 6A, which clearly exhibits three signals. The broad peak at around 40 ppm seen in the MAS spectra is actually composed of two components with isotropic chemical shift values of about 45 (strong) and 55 ppm (weak). On the basis of the previous work,[44−46] we assigned the 45 ppm peak to the tetrahedral Al with $Al(OP)_4$ environment and the 55 pm peak to the tetrahedral Al atoms in aluminosilicate domains with Si as the nearest neighbor. The peak at 6 ppm in the MAS spectrum appears in the F1 dimension with an isotropic chemical shift of 15 ppm, and as mentioned earlier it originates from the unreacted alumina.

Washing the sample with water results in a significant change in the ^{31}P MAS spectra (Figure 3B). The gel samples heated for less than 2 days are X-ray amorphous upon washing. Their corresponding ^{31}P spectra now contain a very broad envelop resulting from many overlapping peaks with a maximum at

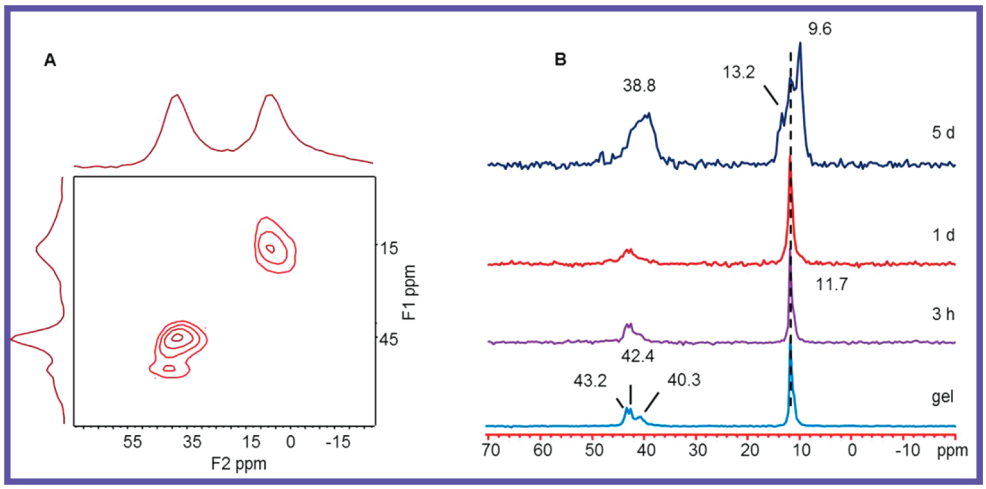

Figure 6. ^{27}Al 3QMAS spectrum of SAC 5d sample (A) and ^{13}C CP MAS spectra of selected unwashed SAC gel samples (B).

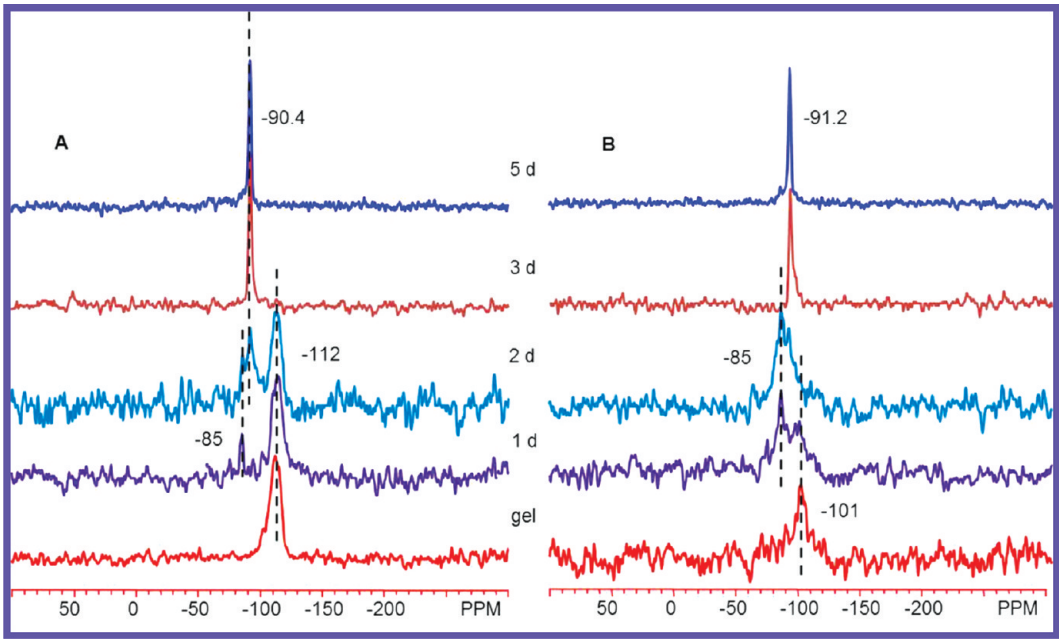

Figure 7. ^{29}Si MAS (A) and ^{1}H → ^{29}Si CP spectra of selected unwashed SAC gel samples with a contact time of 0.5 ms (B).

around −12 ppm and a relative sharp peak at near −20 ppm seen in the unwashed samples. It appears that part of the layered materials transforms to a completely amorphous material with no short-range ordering, but a significant portion of the layered material was able to retain the ordered local P environment, although long-range ordering is lost.

The ^{13}C CP MAS spectra of selected SAC gel samples were obtained to follow the behavior of the SDA molecules inside the gel samples (Figure 6B). The ^{13}C chemical shifts of the methylene and methyl carbons in free DEA molecule are 44.2 and 15.4 ppm, and in a protonated DEA molecule (DEA−H$^+$) the chemical shifts of these two resonances are shifted to 43.6 and 12.2 ppm.[19,47,48] In the ^{13}C CP MAS spectrum of the initial dry gel without heating, the methyl group appears as a relatively sharp peak at 11.7 ppm with a shoulder at around 11 ppm, and the methylene region has three peaks at 43.2, 42.4, and 40.3 ppm. The chemical shift values indicate that the DEA molecules are in a protonated form, and the multiple signals suggest that the protonated DEA−H$^+$ have different environments. The sharpness of the peaks suggests that the SDA located between the layers has high mobility, resulting in a weaker proton−carbon dipolar interaction. In the final SAPO-34 product, the ^{13}C peaks become much broader, and the methyl region has at least four peaks. Such spectrum implies that the DEA−H$^+$ ions in the CHA cages may be disordered: the number of DEA molecule may vary from one to two, and the orientation of the DEA−H$^+$ may differ from cage to cage, both of which depend on the Si distribution. The broad peaks also indicate that the SDA is less mobile once they are trapped inside the CHA cage.

To investigate the Si incorporation, ^{29}Si MAS and ^{1}H → ^{29}Si CP spectra were obtained (Figure 7). The ^{29}Si MAS spectra of the gel samples heated for less than 2 days show that the initial gel only has a single peak at around −112 ppm, which can be assigned to unreacted amorphous silica with Si(OSi)$_4$ environments.[2,30,49,50]

This observation indicates that the vast majority of the silica in the gel has not started reacting, implying that the crystalline and semicrystalline layered phases are mainly AlPO in nature. This result is not surprising because the lack of bulk water will inevitably slow the dissolution of silica. After 2 days of heating, a new peak begins to appear at −90.4 ppm characteristic of $Si(OAl)_4$ environment often observed in SAPOs. This is consistent with the corresponding XRD pattern, SEM image, and ^{31}P MAS spectrum of the 2 d sample showing the appearance of SAPO-34 crystals. The spectrum of final product of SAPO-34 only has a sharp peak at −90.4, which is due to the isolated $Si(OAl)_4$ species in SAPO-34 as was reported previously in HTS.[14−16,18,50]

The $^1H \rightarrow {}^{29}Si$ CP NMR experiments were also carried out. Because CP is a technique that utilizes the $^1H-{}^{29}Si$ dipolar interaction, it can be used for spectral editing. Specifically, CP selectively enhances the intensity of the ^{29}Si nuclides with protons in their close proximity. The CP spectrum of the initial dry gel (Figure 7B) exhibits a relatively weak signal at −101 ppm, which is not clearly visible in the corresponding MAS spectrum. This signal represents a small amount of Si atoms on the surface of silica particles with a chemical environment of $(SiO)_3SiOH$. As mentioned earlier, the strong peak seen in the MAS at −112 ppm is due to the Si in bulk silica with $Si(OSi)_4$ environments. Because this species has no silanol groups directly attached, its signal does not show up in the CP spectra obtained with a very short contact time (0.5 ms). The CP spectra of 1- and 2-day samples show a new peak appearing at around −85 ppm (Figure 7B). The chemical shift of this peak corresponds to $(AlO)_3SiOH$ or $(SiO)(AlO)Si(OH)_2$ in amorphous aluminosilicates.[51] The protons on the silinol groups are the reason that these Si species are seen in the CP spectra. Thus, CP data imply that the SAC treatment leads to the formation of a small amount of amorphous aluminosilicate particles due to the reaction of silica with alumina. This aluminosilicate species further reacts with layered AlPO phase, resulting in Si incorporation upon transforming to SAPO-34. It seems that under the DGC conditions (i.e., the lack of bulk water), forming aluminosilicates is one way to "dissolute" or activate silica for further reaction. This peak disappeared in the final SAPO-34 (3- and 5-day samples), implying they were consumed at the end of crystallization.

Table 1. Elemental Compositions (Molar Basis) of SAPO-34 from EDX Analysis

method	sample	Si	Al	Al	P/Al	(Si + P)/Al
SAC	5 d	0.12	0.50	0.38	0.76	1.00
VPT	7 d	0.16	0.47	0.37	0.79	1.13

In general, there are three Si substitution mechanisms (SM) in $AlPO_4$-based frameworks: (1) Si incorporation into an Al site (SM I), (2) Si incorporation into a P site (SM II), and (3) 2Si for Al + P (SM III).[52] The P/Al ratio in $AlPO_4$-based molecular sieves is strictly 1:1. The change in the P/Al ratio upon Si substitution reflects the mechanisms through which Si is incorporated. EDX analysis was performed to obtain semiqualitative information on elemental composition. The results reported in Table 1 were averaged from the data obtained from at least three different SAPO-34 crystals. The average Si content in SAPO-34 (5 d sample) is about 12 mol %, which is very close to the proposed upper threshold value (11%) of the SM II mechanism in SAPO-34.[53,54] Further, the (Si + P)/Al is equal to 1. Therefore, the EDX data indicate that one Si only substitutes for one P atom (SM II). This argument is supported by the ^{29}Si MAS spectra of SAPO-34, which show only a single peak at about −90 ppm due to the $Si(OAl)_4$ environment.

From the information obtained from both XRD and NMR data, we propose a scheme that quantitatively describes the formation of SAPO-34 under the SAC conditions (Scheme 3). Upon drying the wet gel resulting from mixing Al and P and Si sources as well as DEA, a crystalline layered phase formed immediately. Previous AFM studies showed that the step height of terraces on (001) faces SAPO-34[55] and related STA-7[56] correspond to the tilted double-six-ring (D6R) on the surface, suggesting that the D6R is energetically stable to terminate the structure of SAPO-34 and other frameworks composed of D6Rs on the crystal surface. Thus, we suggest that the layer of the crystalline phase bears a resemblance to the (001) face of SAPO-34 in that it contains titled D6Rs, and they are held together by the weak nonbonding forces. However, the D6R units may not possess the same orientation with respect to the lattice plan as they do on the (001) face of SAPO-34. Upon heating, under the influence of water vapor, the layered phase partially loses its crystallinity and becomes semicrystalline. It is likely accompanied by the slight rearrangement of the tilted D6Rs via bond breaking

Scheme 3. Illustration of the Formation of SAPO-34 under SAC Conditions

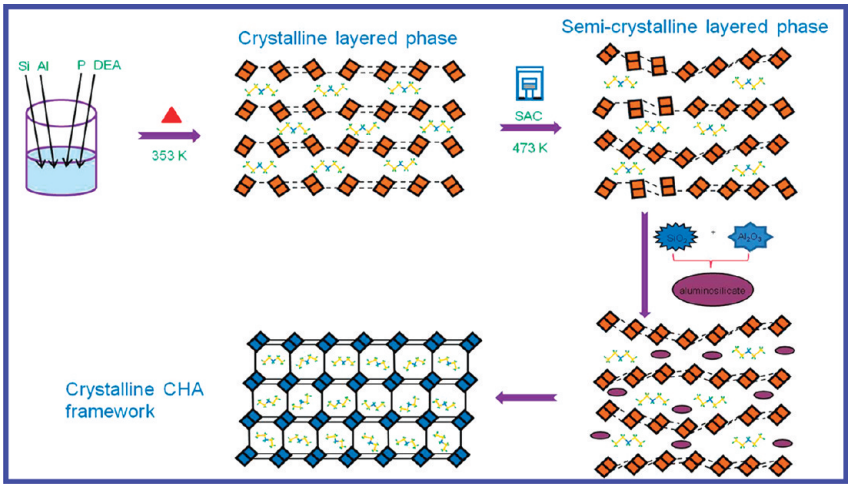

dx.doi.org/10.1021/jp208560t |J. Phys. Chem. C 2011, 115, 22309–22319

and reforming to orientate themselves to the same orientation along the three crystallographic axes. The layered phases are mainly AlPO in nature with little Si. Meanwhile, silica appears to react with alumina under SAC conditions, yielding small aluminosilicate particles presumably dispersed between the AlPO layers. The last step is that the layers are cooperatively cross-linked together forming the CHA cages around protonated DEA cations, yielding the SAPO-34 framework. It is at this stage that the Si atoms are incorporated into the framework as isolated $Si(OAl)_4$ species. The key component of the proposed scheme is that the layers of the intermediates contain D6Rs. Besides the AFM studies of SAPO-34[55] and STA-7[56] mentioned earlier, additional evidence that the D6R is the immediate precursor to the zeolite with FAU topology can be found in the literature.[57,58]

Formation of SAPO-34 under VPT Conditions. The VPT method differs from SAC in that the initial dry gel does not contain SDA. The structure of the initial VPT dry gel without heating is remarkably different from that of the SAC initial dry gel. Its powder XRD pattern indicates that the VPT dry gel is mainly amorphous, but does not necessarily have a layered structure (Figure S2). The ^{31}P MAS spectrum (Figure S3) implies that the P local environments are also different. The corresponding ^{27}Al MAS spectrum (Figure S4) shows that both tetrahedral (38 ppm) and octahedral Al (−14 ppm) exist. The $^{31}P\{^{27}Al\}$ and $^{27}Al\{^{31}P\}$ REDOR data (Figure S5A-B) suggest that the amorphous sample contains mainly an amorphous AlPO phase and some unreacted pseudoboehmite. The SEM image (Figure S6A) shows amorphous aggregates. Such a difference is due to the lack of DEA in the gel.

Interestingly, once the DEA molecules are brought in contact with the gel, a semicrystalline layered phase forms immediately as evidenced by seeing a very broad low angle peak in the powder XRD pattern of 3 h sample. Because the powder XRD pattern and the ^{31}P and ^{27}Al MAS spectra of this sample are almost identical to that of the semicrystalline phase formed during the SAC process (Figures S3,4), it is reasonable to believe that both semicrystalline phases have similar layered structure with the same local P and Al environments. The results indicate that one of the roles of DEA is to promote the formation of the layered AlPO phase. For this semicrystalline phase formed under VPT conditions, the changes in the PXRD, ^{31}P, ^{27}Al, and ^{13}C NMR spectra as a function of time follow the same tends as seen during the SAC process (Figures S2−4 and S7B). Formation of a small amount of $AlPO_4$-11 as a competing phase is also observed in the early stage of the crystallization. The PXRD pattern and NMR spectra of washed samples confirm that the semicrystalline phase is also held by weak nonbonding interactions (Figures S2B and S3B). The final product (7 d sample) is fairly pure without $AlPO_4$-11. The corresponding SEM image (Figure S6D) shows well-crystallized SAPO-34 with trigonal morphology. The ^{27}Al 3QMAS spectrum (Figure S7A) of 7 d sample is also the same as that of the SAPO-34 obtained from the SAC method, and the $^{27}Al\{^{31}P\}$ REDOR difference spectrum (Figure S5C) shows that SAPO-34 only has tetrahedral Al.

Similar to SAC, ^{29}Si MAS and $^{1}H \rightarrow {}^{29}Si$ CP NMR spectra (Figure S8) reveal that the Si incorporation occurs through the mechanism very similar to that observed during the SAC process; that is, the silica is activated via formation of aluminosilicate species. The spectrum of final SAPO-34 has a sharp peak at −91 ppm representing $Si(OAl)_4$ species. There is also a small peak at −95 ppm. This peak is associated with a small amount of $Si(OAl)_3(OSi)$ species. The EDX results are given in Table 1. The (Si + P)/Al ratio (1.13) and the Si content (16%) indicate that, in addition to isolated $Si(OAl)_4$ species, a very small amount of Si island also exist, which is consistent with the small Si peak at −95 ppm.

To gain further information regarding the nucleation and growth, the surface morphology of SAPO-34 was examined by AFM. In recent years, AFM has emerged as a powerful technique to study the crystallization of microporous materials due to its nanometer scale resolution of surface feature.[59−62] Recently, growth mechanisms of SAPO-34 under hydrothermal synthesis conditions with morpholine as SDA were examined,[55] and the results provide a benchmark for interpretation of our data.

Figure 8A shows the SEM image of SAPO-34 prepared by the VPT approach. On the basis of the crystal morphology and the recent AFM work on SAPO-34 prepared by HTS,[55] the crystal surface can be assigned to the (001) face of the rhombohedral unit cell. For the SAPO-34 samples prepared by DGC methods, the crystal surfaces are often covered by a significant amount of surface debris even after extensive washing. Therefore, finding the crystals with good surface conditions suitable for AFM analysis is very challenging and time-consuming. Nonetheless, we were able to find few crystals with relatively good surface conditions. The AFM images of one of such crystals are shown in Figure 8B (because the topographic image has a large height range, which obscures the visualization of the crystals having small height differences, we show the error signal image for clarity). As the maximum scanning area of the AFM instrument used ($45 \times 45\ \mu m^2$) is smaller than the crystal face, four AFM images of (001) face containing four corners from the same crystal were recorded separately, and piecing them together provides the outline of the 2D surface (Figure 8B). "Pseudo-rectangular" terraces parallel to [100] and [010] directions can be found at several locations on the same crystal surface (two such terraces are shown inside the blue box inside Figure 8B). The spiral growth was previously observed on the (001) surface of the SAPO-34 crystals synthesized with morpholine under HTS conditions,[55] but no such spiral was found for the SAPO-34 crystals prepared by the VPT method. The magnified image (Figure 8C) shows the rough surface and multiple nucleation points on the surface, suggesting that the crystal growth mechanism is "birth and spread".[62] Under VPT conditions employed in this study, the nucleation rate appears to be fast as is evident from many nuclei on the crystal surface. These nuclei quickly spread and coalesce to form terraces.

Analysis of cross-section profiles for four individual freshly formed nuclei sitting on relatively flat terraces (the ones inside red circles in Figure 8C) shows that the average height of the nuclei is 22 nm (Figure 8D,E shows the cross-sectional depth profile of two such nuclei). There are several nuclei (see the ones inside blue circles in Figure 8C) whose heights are about 10 nm. However, these nuclei have already partially merged with the terraces underneath.

The average nuclei height is 22 nm, which is much larger than that (0.9 nm) found for the crystals synthesized by HTS method.[55] SAPO-34 structure is built upon the D6Rs joint together via single four-membered rings. As mentioned earlier, the height of the terrace (0.9 nm) reported corresponds to the repeat distance (0.94 nm) between the layers of the tilted D6Rs along the [001] direction. In the present work, the average height of nuclei formed under VPT conditions is 22 nm, corresponding to about 23 layers of D6Rs.

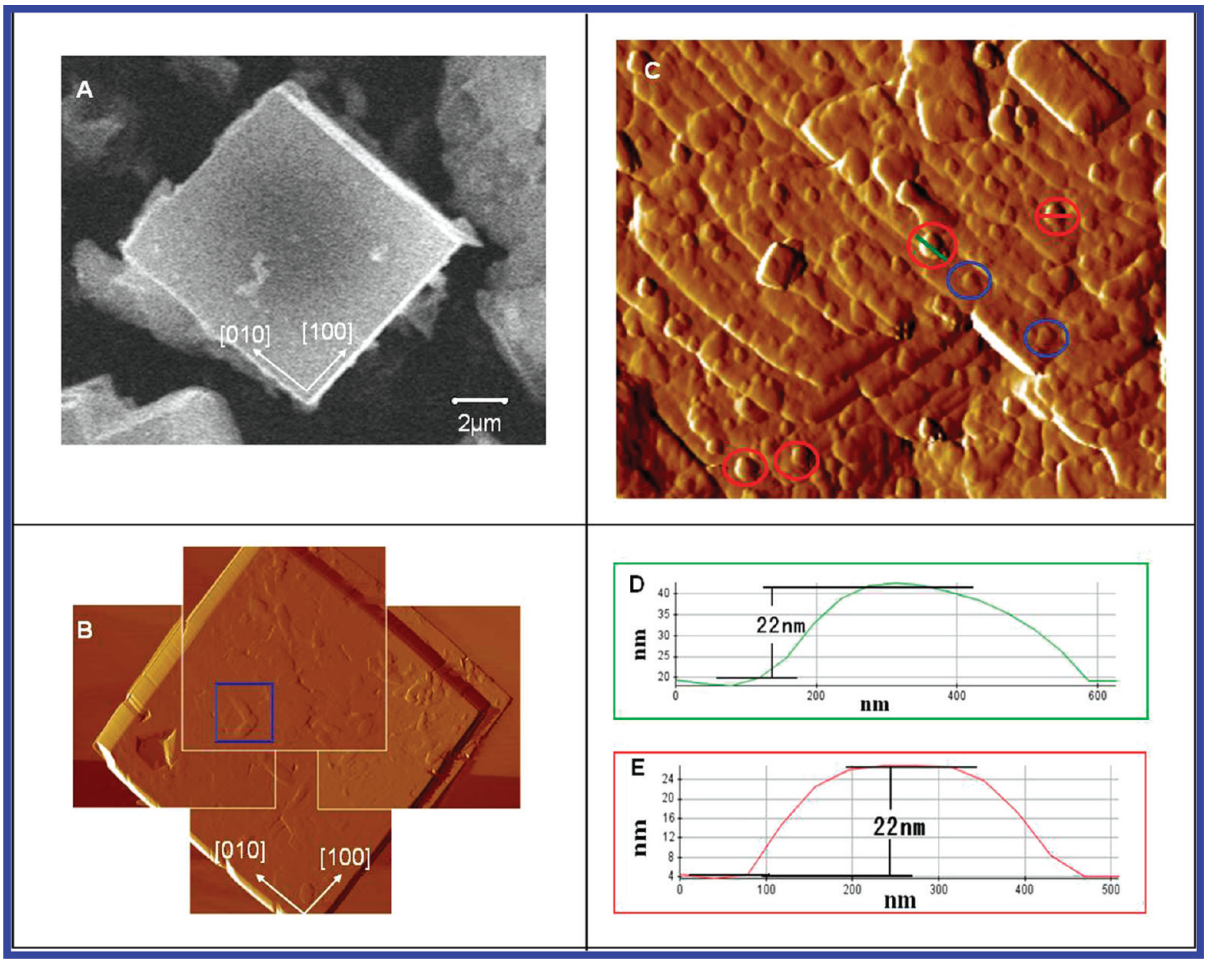

Figure 8. SEM and AFM images of the (001) face of SAPO-34 crystals (VPT 7 d sample): (A) SEM image of a crystal; (B) top-view AFM images (error signals are shown here for clarity) of another large crystal, each image taken in size of $45 \times 45\,\mu m^2$; (C) enlarged view of a square area in (B), $10 \times 10\,\mu m^2$; and (D,E) cross-section height profile from the topographic image (not shown) along different lines as shown in (C), showing the height of two nuclei.

Scheme 4. Illustration of Nucleus Formation on the (001) Face[a]

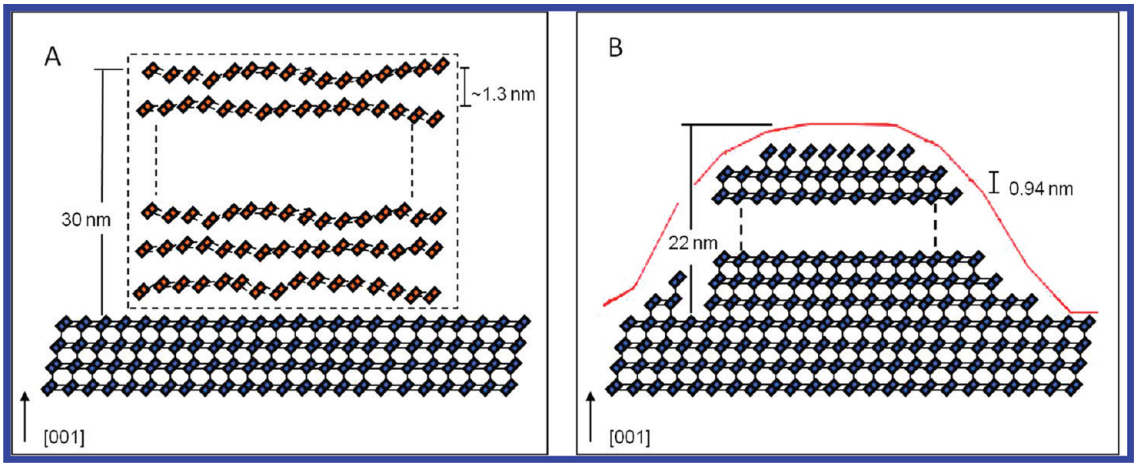

[a] (A) 23 sheets of precursor with a total height of about 30 nm; (B) a SAPO-34 nucleus containing 23 layers of D6Rs with a height of 22 nm.

The AFM results provide some details that can be included in the SAPO-34 formation mechanism under DGC conditions proposed earlier. Unlike hydrothermal synthesis where nutrients can come from the liquid phase, all of the reactive species in DGC are contained in the solid phases. The small amount of bulk water is separated from the dry gel, which eliminates the direct contact

between the reactive species in solution and solid gel. The small amount of water in vapor is not enough to dissolve the solids. Therefore, the formation of SAPO-34 is unlikely through gel dissolution, and therefore the single D6R layer growth was not observed because the bulk liquid containing the immediate precursor such as D6R unit is lacking. Therefore, SAPO-34 is likely formed through the conversion of the layered precursor, which already has the sheet of tilted D6Rs in the layer. As mentioned earlier, the forces holding the sheets together are weak nonbonding interactions, which facilitate bond breaking and reforming in the absence of bulk liquid and therefore assist in the transformation from the layered phase to SAPO-34. Such transformation might occur in a small domain involving several sheets of D6Rs in the precursor at once via cooperative reorganization of local structure of P and Al as well as Si species in the vicinity. The number of the sheet in the precursor involved in each domain may be estimated from PXRD and AFM data. From the PXRD pattern of 3 h sample, the interlayer spacing can be estimated at 1.3 nm. Thus, observed nuclei with a height of 22 nm, corresponding to 23 layers of D6Rs in SAPO-34, may result from the simultaneous transformation of 23 sheets of precursor (with a total height of 30 nm). Such a nucleation process is illustrated in Scheme 4. Seeing many nuclei in Figure 8C indicates that the transformation happens in many locations within the precursor.

SUMMARY

We have examined the formation of SAPO-34 under the DGC conditions. The evolution of the solid gel phase as a function of heating time was followed by PXRD and solid-state NMR. Crystallization pathways appear to be the same under the SAC and VPT conditions for SAPO-34. SAPO-34 crystallizes from a semicrystalline precursor. This precursor has a layered structure held together by weak nonbonding interactions. Although the observation that the formation processes under SAC and VPT are the same is not totally surprising, the VPT experiment does indicate that DEA promotes the formation of the layered intermediate. The AFM data suggest that nucleation occurs through simultaneous conversion of the domains within the precursor to SAPO-34. The crystal growth follows the "birth and spread" mechanism. The Si NMR results indicate that the silica first reacts with alumina to form a more reactive alminosilicate species before Si being incorporated into the framework. A combination of the data obtained from different techniques provides a better picture of the formation of SAPO-34.

ASSOCIATED CONTENT

Supporting Information. $^{31}P\{^{27}Al\}$ REDOR spectrum of unwashed 3 h SAC sample, powder XRD patterns of dry gel samples synthesized under VPT conditions, and corresponding NMR spectra of selected samples (eight figures). This material is available free of charge via the Internet at http://pubs.acs.org.

AUTHOR INFORMATION

Corresponding Author
*E-mail: yhuang@uwo.ca.

ACKNOWLEDGMENT

Y.H. thanks the Natural Science and Engineering Research Council of Canada for a research grant and the Canada Foundation for Innovation for an equipment grant. Funding from the Canada Research Chair program is also gratefully acknowledged. We sincerely thank Prof. X. Sun (UWO) for generously allowing us to use his SEM instrument and Ms. R. Li (UWO) for her kind help with the SEM and EDX measurements.

REFERENCES

(1) Yu, J.; Xu, R. *Chem. Soc. Rev.* **2006**, *35*, 593–604.
(2) Prakash, A. M.; Unnikrishnan, S. *J. Chem. Soc., Faraday Trans.* **1994**, *90*, 2291–2296.
(3) Li, S.; Falconer, J. L.; Noble, R. D. *J. Membr. Sci.* **2004**, *241*, 121–135.
(4) Wragg, D. S.; Johnsen, R. E.; Norby, P.; Fjellvag, H. *Microporous Mesoporous Mater.* **2010**, *134*, 210–215.
(5) Song, W.; Nicholas, J. B.; Haw, J. F. *J. Phys. Chem. B* **2001**, *105*, 4317–4323.
(6) Song, W.; Fu, H.; Haw, J. F. *J. Am. Chem. Soc.* **2001**, *105*, 4749–4754.
(7) Wu, X.; Abraha, M. G.; Anthony, R. G. *Appl. Catal., A* **2004**, *260*, 63–69.
(8) Hereijgers, B. P. C.; Bleken, F.; Nilsen, M. H.; Svelle, S.; Lillerud, K. P.; Bjorgen, M.; Weckhuysen, B. M.; Olsbye, U. *J. Catal.* **2009**, *264*, 77–87.
(9) Vora, B.; Chen, J. Q.; Bozzano, A.; Glover, B.; Barger, P. *Catal. Today* **2009**, *141*, 77–83.
(10) Liu, Z.; Liang, J. *Curr. Opin. Solid State Mater. Sci.* **1999**, *4*, 80–84.
(11) Vistad, Ø. B.; Hansen, E. W.; Akporiaye, D. E.; Lillerud, K. P. *J. Phys. Chem. A* **1999**, *103*, 2540–2552.
(12) Vistad, Ø. B.; Akporiaye, D. E.; Lillerud, K. P. *J. Phys. Chem. B* **2001**, *105*, 12437–12447.
(13) Yan, Z.; Chen, B.; Huang, Y. *Solid State Nucl. Magn. Reson.* **2009**, *35*, 49–60.
(14) Xu, L.; Du, A.; Wei, Y.; Wang, Y.; Yu, Z.; He, Y.; Zhang, X.; Liu, Z. *Microporous Mesoporous Mater.* **2008**, *115*, 332–337.
(15) Liu, G.; Tian, P.; Zhang, Y.; Li, J.; Xu, L.; Meng, S.; Liu, Z. *Microporous Mesoporous Mater.* **2008**, *114*, 416–423.
(16) Tan, J. L. J.; Bao, X.; Liu, X.; Han, X.; He, C.; Zhai, R. *Microporous Mesoporous Mater.* **2002**, *53*, 97–108.
(17) Vistad, Ø. B.; Akporiaye, D. E.; Taulelle, F.; Lillerud, K. P. *Chem. Mater.* **2003**, *15*, 1639–1649.
(18) Liu, G.; Tian, P.; Li, J.; Zhang, D.; Zhou, F.; Liu, Z. *Microporous Mesoporous Mater.* **2008**, *111*, 143–149.
(19) Tian, P.; Su, X.; Wang, Y.; Xia, Q.; Zhang, Y.; Fan, D.; Meng, S.; Liu, Z. *Chem. Mater.* **2011**, *23*, 1406–1413.
(20) Kim, M. H.; Li, H. X.; Davis, M. E. *Microporous Mater.* **1993**, *1*, 191–200.
(21) Xu, W.; Dong, J.; Li, J.; Li, J.; Wu, F. *J. Chem. Soc., Chem. Commun.* **1990**, *10*, 755–756.
(22) Bandyopadhyay, R.; Bandyopadhyay, M.; Kubota, Y.; Sugi, Y. *J. Porous Mater.* **2002**, *9*, 83–95.
(23) CN Patent 1,314,587C.
(24) Hirota, Y.; Murata, K.; Tanaka, S.; Nishiyama, N.; Egashira, Y.; Ueyama, K. *Mater. Chem. Phys.* **2010**, *123*, 507–509.
(25) Zhang, L.; Yao, J.; Zeng, C.; Xu, N. *Chem. Commun.* **2003**, *17*, 2232–2233.
(26) Yao, J.; Wang, H.; Ringer, S. P.; Chan, K. Y.; Zhang, L.; Xu, N. *Microporous Mesoporous Mater.* **2005**, *85*, 267–272.
(27) Khan, N. A.; Park, J. H.; Jhung, S. H. *Mater. Res. Bull.* **2010**, *45*, 377–381.
(28) Yang, H.; Liu, Z.; Gao, H.; Xie, Z. *J. Mater. Chem.* **2010**, *20*, 3227–3231.
(29) Bandyopadhyay, M.; Bandyopadhyay, R.; Tawada, S.; Kubota, Y.; Sugi, Y. *Appl. Catal., A* **2002**, *225*, 51–62.
(30) Chen, B.; Huang, Y. *Microporous Mesoporous Mater.* **2009**, *123*, 71–77.

(31) Matsukata, M.; Ogura, M.; Osaki, T.; Rao, P. R. H. P.; Nomura, M.; Kikuchi, E. *Top. Catal.* **1999**, *9*, 77–92.
(32) Cundy, C. S.; Cox, P. A. *Chem. Rev.* **2003**, *103*, 663–702.
(33) Gullion, T.; Schaefer, J. *J. Magn. Reson.* **1989**, *81*, 196–200.
(34) Huang, Y.; Richer, R.; Kirby, C. W. *J. Phys. Chem. B* **2003**, *107*, 1326–1337.
(35) Amoureux, J. P.; Fernandez, C.; Steuernagel, S. *J. Magn. Reson., Ser. A* **1996**, *123*, 116–118.
(36) Tapp, N.; Milestone, N.; Bibby, D. *Zeolites* **1988**, *8*, 183–188.
(37) Chen, B.; Huang, Y. *J. Am. Chem. Soc.* **2006**, *128*, 6437–6446.
(38) Chen, B.; Huang, Y. *J. Phys. Chem. C* **2007**, *111*, 15236–15243.
(39) Chen, B.; Kirby, C. W.; Huang, Y. *J. Phys. Chem. C* **2009**, *113*, 15868–15876.
(40) Chen, B.; Huang, Y. *Microporous Mesoporous Mater.* **2011**, *143*, 14–21.
(41) Huang, Y.; Yan, Z. *J. Am. Chem. Soc.* **2005**, *127*, 2731–2740.
(42) Zhou, D.; Xu, J.; Yu, J.; Chen, L.; Deng, F.; Xu, R. *J. Phys. Chem. B* **2006**, *110*, 2131–2137.
(43) Huang, Y.; Demko, B. A.; Kirby, C. W. *Chem. Mater.* **2003**, *15*, 2437–2444.
(44) Akporiaye, D. E.; Dahl, I. M.; Mostad, H. B.; Wendelbo, R. *J. Phys. Chem.* **1996**, *100*, 4148–4153.
(45) Prakash, A. M.; Unnikrishnan, S.; Rao, K. V. *Appl. Catal., A* **1994**, *110*, 1–10.
(46) Yan, Z.; Zhuang, J.; Xu, L.; Han, X.; Liu, Z.; Bao, X. *Chin. Chem. Lett.* **2003**, *14*, 87–90.
(47) Sarneski, J. E.; Surprenant, H. L.; Molen, F. K.; Reilley, C. N. *Anal. Chem.* **1975**, *47*, 2116–2124.
(48) Challoner, R.; Harris, R. K.; Packer, K. J.; Taylor, M. J. *Zeolites* **1990**, *10*, 539–545.
(49) Ye, L.; Cao, F.; Ying, W.; Fang, D.; Sun, Q. *J. Porous Mater.* **2011**, *18*, 225–232.
(50) Ashtekar, S.; Chilukuri, S. V. V.; Chakrabarty, D. K. *J. Phys. Chem.* **1994**, *98*, 4878–4883.
(51) Doremieux-Morin, C.; Martin, C.; Bregeault, J. M.; Fraissard, J. *Appl. Catal.* **1991**, *77*, 149–161.
(52) Sastre, G.; Lewis, D. W.; Richard, C.; Catlow, A. *J. Phys. Chem. B* **1997**, *101*, 5249–5262.
(53) Vomscheid, R.; Briend, M.; Peltre, M. J.; Man, P. P.; Barthomeuf, D. *J. Phys. Chem.* **1994**, *98*, 9614–9618.
(54) Barthomeuf, D. *J. Phys. Chem.* **1993**, *97*, 10092–10096.
(55) Holme, B.; Cubillas, P.; Cavka, J. H.; Slater, B.; Anderson, M. W.; Akporiaye, D. *Cryst. Growth Des.* **2010**, *10*, 2824–2828.
(56) Cubillas, P.; Castro, M.; Jelfs, K. E.; Lobo, A. J. W.; Slater, B.; Lewis, D. W.; Wright, P. A.; Stevens, S. M.; Anderson, M. W. *Cryst. Growth Des.* **2009**, *9*, 4041–4050.
(57) Melchior, M. T.; Vaughan, D. E. W; Pictroski, C. F. *J. Phys. Chem.* **1995**, *99*, 6128–6144.
(58) Wakihara, T.; Sugiyama, A.; Okubo, T. *Microporous Mesoporous Mater.* **2004**, *70*, 7–13.
(59) Ono, S. S.; Matsuoka, O.; Yamamoto, S. *Microporous Mesoporous Mater.* **2001**, *48*, 103–110.
(60) Anderson, M. W. *Curr. Opin. Solid State Mater. Sci.* **2001**, *5*, 407–415.
(61) Paredes, J. I.; Martinez-Alonso, A.; Tascon, J. M. D. *Microporous Mesoporous Mater.* **2003**, *65*, 93–126.
(62) Cubillas, P.; Anderson, M. W. In *Zeolites and Catalysis: Synthesis, Reactions and Applications*, 1st ed.; Čejka, J., Corma, A., Zones, S., Eds.; Wiley-VCH: Weinheim, Germany, 2010; Vol. 1, pp 1−55.